

6.3

THE LAGRANGE TORANDO DURING VORTEX2. PART II: PHOTOGRAMMETRY ANALYSIS OF THE TORNADO COMBINED WITH DUAL-DOPPLER RADAR DATA

Nolan T. Atkins^{*}, Roger M. Wakimoto[#], Anthony McGee^{*}, Rachel Ducharme^{*}, and Joshua Wurman⁺

^{*}Lyndon State College
Lyndonville, VT 05851

[#]National Center for Atmospheric Research
Boulder, CO 80305

⁺Center for Severe Weather Research
Boulder, CO 80305

1. INTRODUCTION

Over the years, mobile ground-based and airborne Doppler radars have collected high-resolution data within the hook region of supercell thunderstorms (e.g., Bluestein et al. 1993, 1997, 2004, 2007a&b; Wurman and Gill 2000; Alexander and Wurman 2005; Wurman et al. 2007b&c). These studies have revealed details of the low-level winds in and around tornadoes along with radar reflectivity features such as weak echo holes and multiple high-reflectivity rings. There are few

studies, however, that have related the velocity and reflectivity features observed in the radar data to the visual characteristics of the condensation funnel, debris cloud, and attendant surface damage (e.g., Bluestein et al. 1993, 1197, 204, 2007a&b; Wakimoto et al. 2003; Rasmussen and Straka 2007).

This paper is the second in a series that presents analyses of a tornado that formed near LaGrange, WY on 5 June 2009 during the Verification on the Origins of Rotation in Tornadoes Experiment (VORTEX 2). VORTEX 2 (Wurman et al.

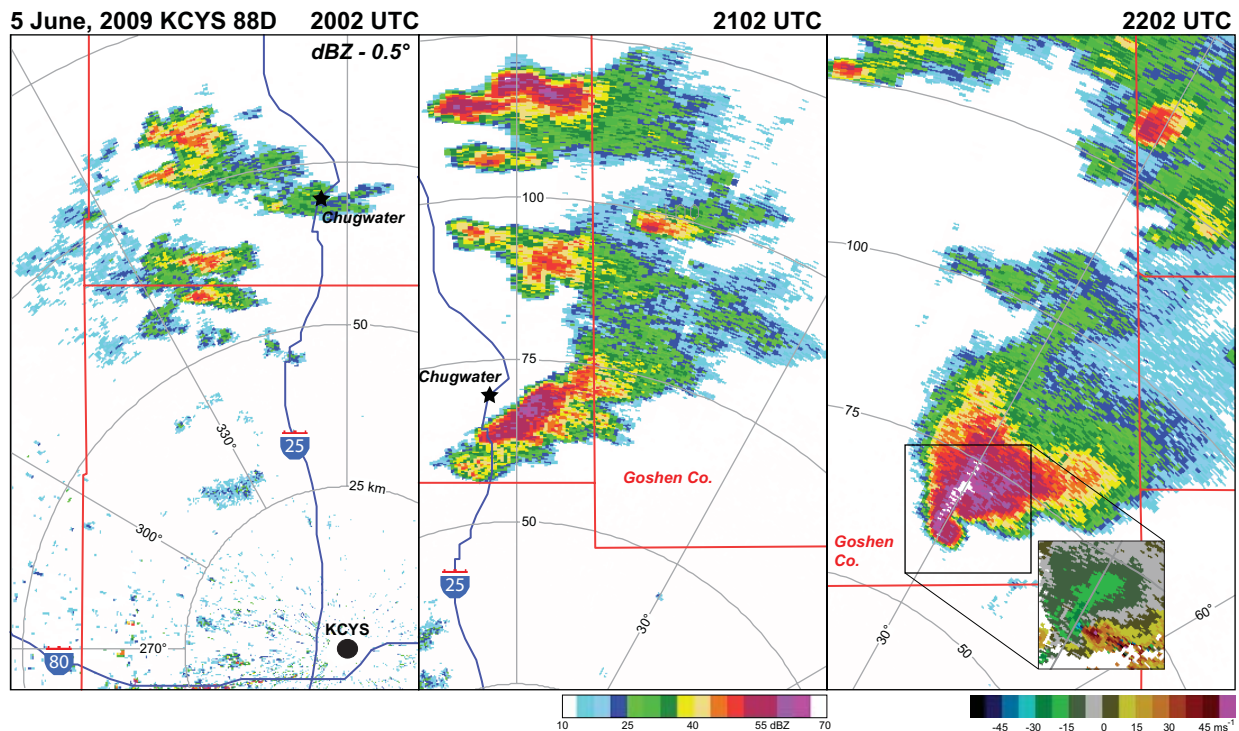


Fig. 1. Radar reflectivity (dBZ) collected by the WSR-88D radar in Cheyenne, WY at 2002, 2102, and 2202 UTC. All data are at an elevation angle of 0.5 degrees. Single-Doppler velocities are shown in the inset panel at 2202 UTC.

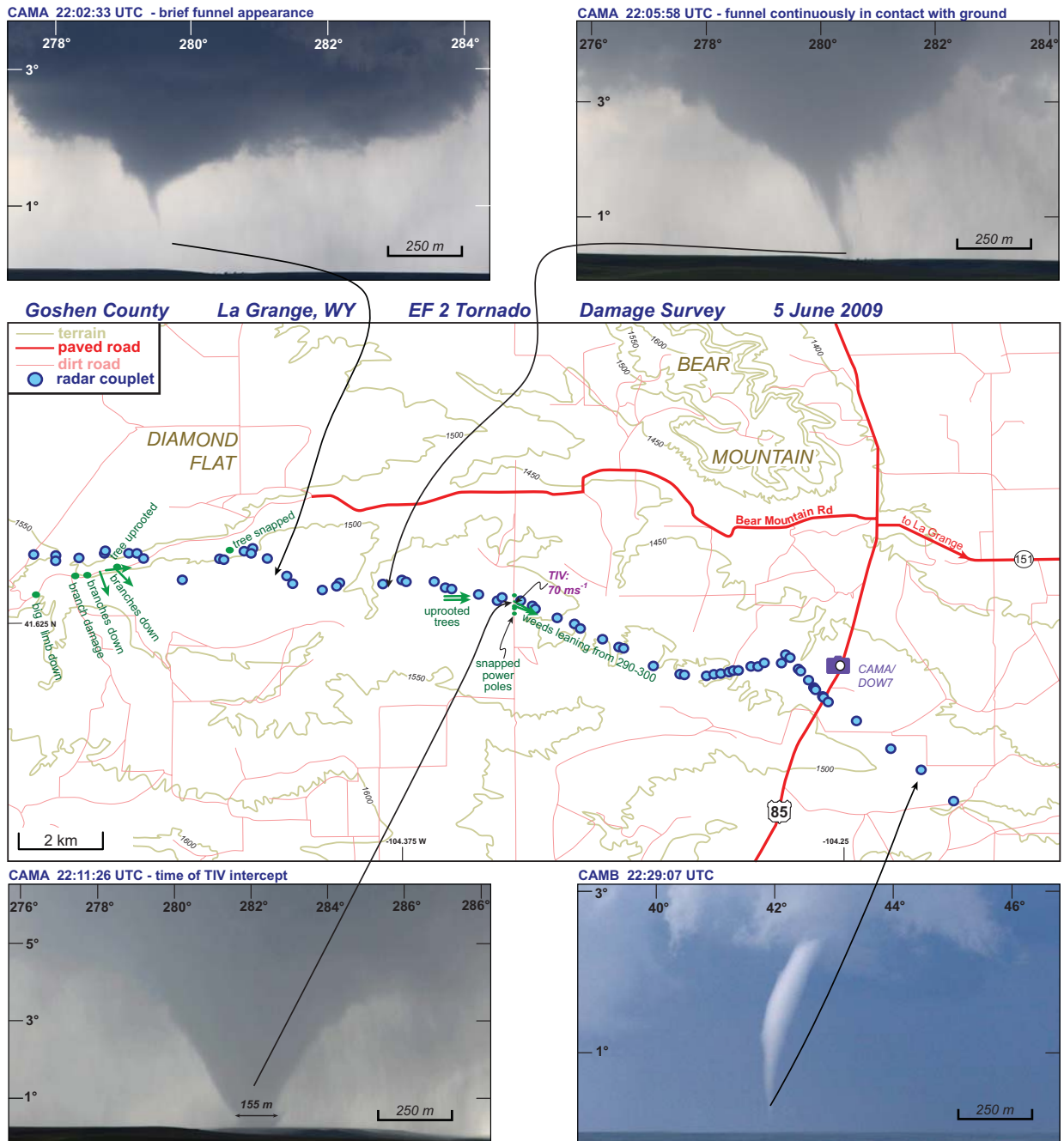


Fig. 2. Photographs at 22:02:33, 22:05, 22:11:26, and 22:29:07 UTC of the LaGrange tornado. All photos except for the one at 22:29:07 UTC were taken at the CAMA/DOW 7 position shown in the central panel. The 22:29:07 UTC photo was taken at the CAMB/DOW 6 position located on Highway 85 southwest of the CAMA/DOW 7 location by about 15 km (not shown). The photos have been reduced or enlarged to ensure the azimuthal spatial distances are the same. Central panel shows locations of damage (green) and the location of the radial velocity couplet (blue).

2010) was a large multi-agency field program that focussed on collecting high-resolution observations of tornadic thunderstorms from 10 May - 13 June, 2009. The experiment featured a large number of mobile *in-situ* and remote sensing observing facilities along with a number of photo teams documenting the visual evolution of the storm.

2. Data Sets and Methodology

The data sets examined in this study include the dual-Doppler data collected by the Doppler on Wheels (DOW 6 and 7; Wurman 2001) radars and a series of photographs collected by the Lyndon State College (LSC) and National Center for Atmospheric Research (NCAR) photography teams. The DOWs collected dual-Doppler data well before tornadogenesis, and subsequently captured much of the tornado evolution.

The DOW 6 and 7 data were interpolated to a cartesian grid with horizontal and vertical grid spacing of 100 m. The horizontal grid was 15 km x 15 km in size. Volume scans were completed every two minutes. Data were collected at elevation angles ranging from 0.5 to 16.0 degrees. The data were objectively analyzed using a Barnes two-pass technique. The motion of the mesocyclone or tornado (when present) was used to correct the data positions and to compute storm relative winds. The three-dimensional wind syntheses were performed using the variational technique as described by Gamache (1997). This variational method minimizes a cost function that considers the radial velocity projections, mass continuity, a lower boundary condition ($w = 0 \text{ ms}^{-1}$ at $z = 0 \text{ m}$) and a smoothing parameter (Frame et al. 2009).

The photography teams documented the low-level cloud features from approximately 20 minutes prior to tornadogenesis through the time the condensation funnel dissipated. Selected photos were chosen for photogrammetric analysis. Cloud photogrammetry is the technique of superimposing the azimuth-elevation angle grid on the photograph relative to the photographer position so as to extract quantitative information about the visual features of the supercell hook region. To perform the analysis, the precise location of at least one landmark relative to the photographer is required, along with a 360 degree panorama shot at the photo position. Spherical trigonometry is then used to compute the

effective focal length and tilt angle of the camera lens. Lens distortion was found to be negligible. Once the effective focal length and tilt angle are computed, azimuths of at least two land marks in the photograph are used to compute the azimuth-elevation angle grid. By cross checking with known positions of landmarks, the grid error is estimated to be no greater than 0.2 degrees. More details on the photogrammetry process can be found in Abrams (1952), Holle (1986), Rasmussen et al. (2003), and Zehnder et al. (2007).

The objective of part II of this study is to combine the dual-Doppler data with the visual features of the wall cloud, condensation funnel, and attendant debris in an effort to better understand the kinematic and reflectivity features observed in the high-resolution Doppler data of the supercell hook region.

3. Storm Evolution and Damage Survey

Fig. 1 shows a time series of radar reflectivity collected by the Cheyenne, WY WSR-88D. Storms began to initiate in southeasterly up slope flow west of Chugwater, WY (Fig. 1a). By 2102 UTC (Fig. 1b), the convection had continued to intensify and a number of supercells had developed and were observed moving to the east-southeast. The VORTEX 2 armada targeted the southern cell as it continued to increase in size and intensity. It was also the easiest cell to target as the terrain in southeastern WY is quite hilly and the road network is sparse. One hour later (2202 UTC), the supercell had moved into Goshen County and had developed a well-defined hook echo and mesocyclone. The velocity differential across the low-level couplet was estimated to be 95 ms^{-1} at 2202 UTC. Note that the reflectivity data shown in Fig. 1c is a few minutes after tornadogenesis, estimated to be about 2154 UTC based on DOW data.

A summary of the visual evolution of the wall cloud, condensation funnel and surface damage is shown in Fig. 2. A photograph taken at the CAMA/DOW 7 location (see central panel for location) at approximately the same time shown in Fig. 1c is presented in Fig 2 at 22:02:33 UTC. At this time, a narrow rope cloud was first observed below the wall cloud base but did not extend to the ground. Thereafter, the rope cloud quickly dissipated. Approximately three minutes later (22:05:58 UTC),

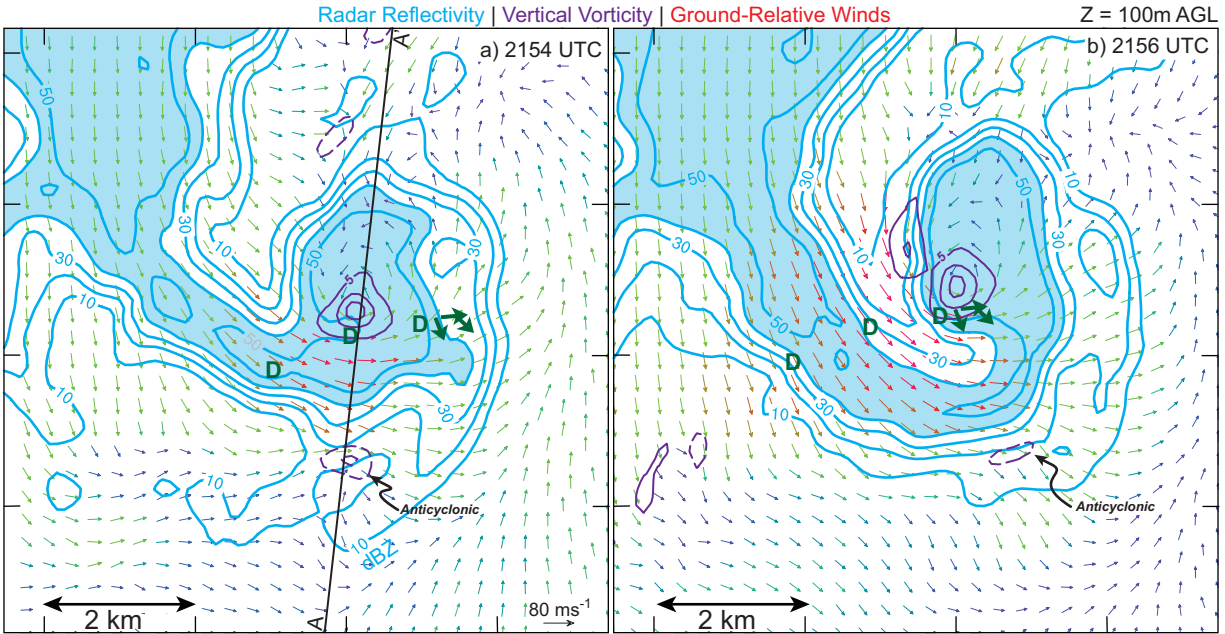


Fig. 3. Radar reflectivity (blue), vertical vorticity (purple; $\times 10^{-2} \text{ s}^{-1}$), ground relative winds (vector field), and damage locations (green) are shown at (a) 2154 UTC and (b) 2156 UTC. All radar fields are at 100 m above ground level (AGL). The cross section location in (a) is shown in Fig. 4.

a condensation funnel had reformed and was observed in contact with the ground. No funnel cloud was observed in contact with the ground from 21:54 UTC (radar-determined tornadogenesis) to 22:05:58 UTC.

The tornado moved to the east southeast at a speed of about 9 ms^{-1} . The funnel continued to widen and at 22:11:26 UTC, it was about 155 m in diameter just above the ground. The funnel diameter continued to widen until approximately 22:18 UTC and subsequently narrowed to a rope-like feature at 22:29:07 UTC. The funnel dissipated completely one minute later.

Post-event ground and aerial damage surveys were performed to assess the extent and severity of the damage. Results of the damage survey are shown in the central panel of Fig. 2. The first damage was produced at about 21:54 UTC, the time coinciding with tornadogenesis. The damage intensity was weak with only a few tree limbs damaged along with an uprooted and snapped tree. As the tornado moved to the east-southeast, a few more trees were uprooted and four power poles were snapped. At the location of the snapped power poles, the Tornado Intercept Vehicle (TIV) measured an *in-situ* wind about approximately 70

ms^{-1} . No other damage was observed with this tornado. It should be noted that the terrain shown in Fig. 2 is rather hilly along the tornado path and the vegetation was sparse, short, and resisted being scoured by the tornadic winds. Based on the limited damage indicators, however, the tornado was rated EF 2 by the National Weather Service.

4. Initial Damage and Vortex Line Analysis

Dual-Doppler data at 2154 and 2156 UTC is shown in Fig. 3. This time was chosen as it appears to be the time when the initial tree damage shown in Fig. 2 was produced. At 2154 UTC (Fig. 3a), the damage locations appear to be located just south of the east-southeastward moving vortex and within the rear-flank downdraft. Notice also the vertical vortex couplet, evident in the vertical vorticity field. The couplet appears to straddle the rear-flank downdraft (Markowski et al. 2008). Two minutes later (Fig. 3b), the hook echo has continued to wrap up. The damage is again located on the southern flank of the vortex. The rear flank downdraft continued to surge eastward.

A vertical cross section through the vortex couplet and hook echo is shown in Fig. 4. Visually, two

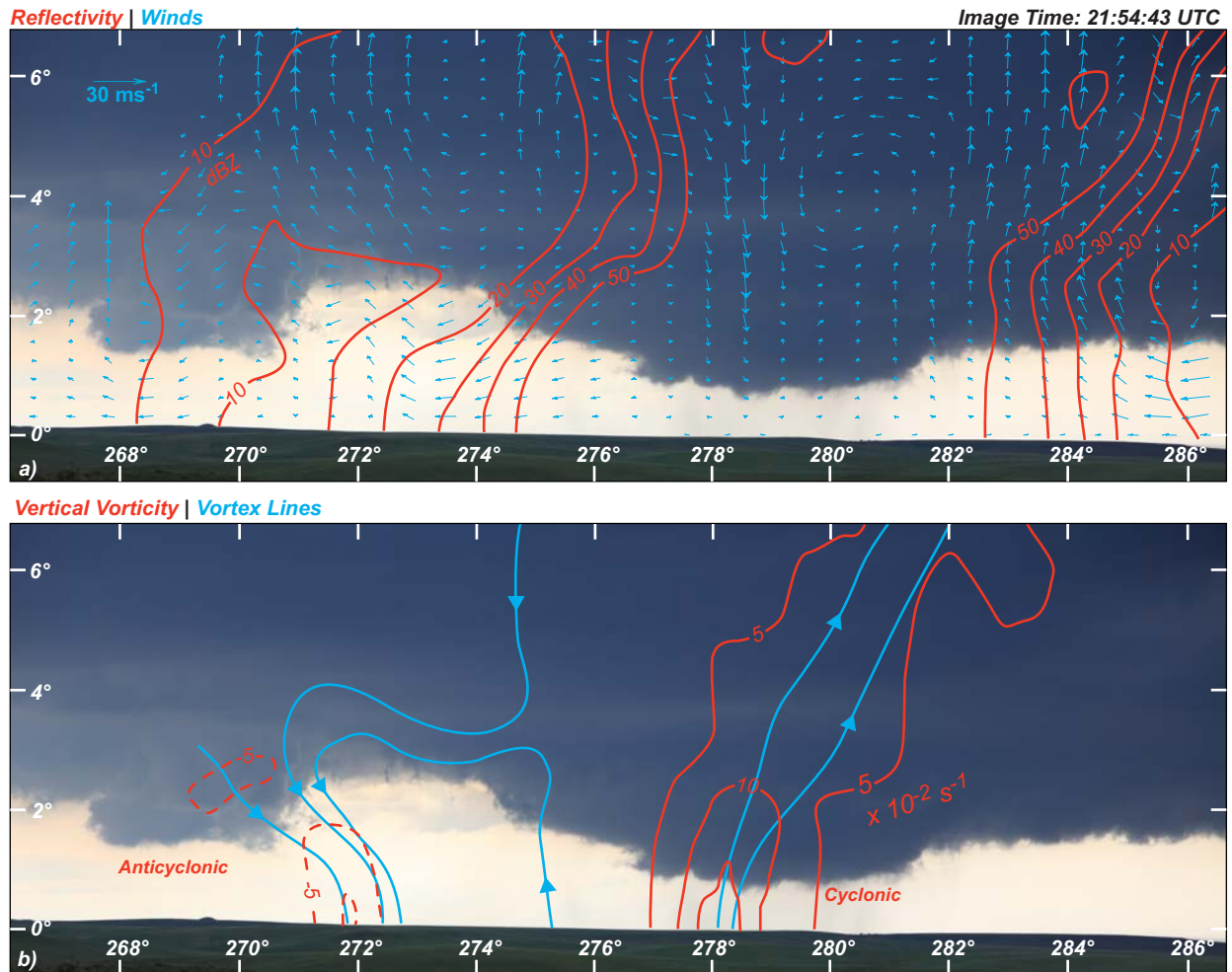


Fig 4. Vertical cross section of dual-Doppler data superimposed on a photograph taken at the DOW7/ CAMA position at 21:54:43 UTC. (a) Radar reflectivity (red) and winds in the plane of the cross section (light blue). (b) Vortex lines (blue) and vertical vorticity (red) Dashed and solid vertical vorticity contours are negative and positive, respectively. Cross section location is shown in Fig. 3a.

lowered cloud bases were observed. The more apparent cyclonic lowering was located at approximately 278 - 280 degrees from the DOW7/CAMA position (Fig. 4a). A maximum of vertical vorticity was collocated with this lowering with the largest values at the ground. The vertical vorticity column appears to tilt northward, a result also observed at other analysis times (not shown). This lowering was also collocated with the higher reflectivities in the hook echo (Fig. 3a). Also apparent is the axial downdraft within the low-level mesocyclone that does not quite reach the surface.

An anticyclonic lowering was also observed at azimuths of approximately 268 - 270 degrees. This lowering was collocated with a maximum of negative vertical vorticity (Fig. 3a and 4b). High-definition video (not shown) confirmed that this feature was indeed rotating anticyclonically.

A recent study by Markowski et al. (2008) showed that the vortex line distribution within the hook region of some supercells formed arches. The arches originated in the cyclonic mesocyclone and pointed upward. They turned southward and continuously descended into the anticyclonic

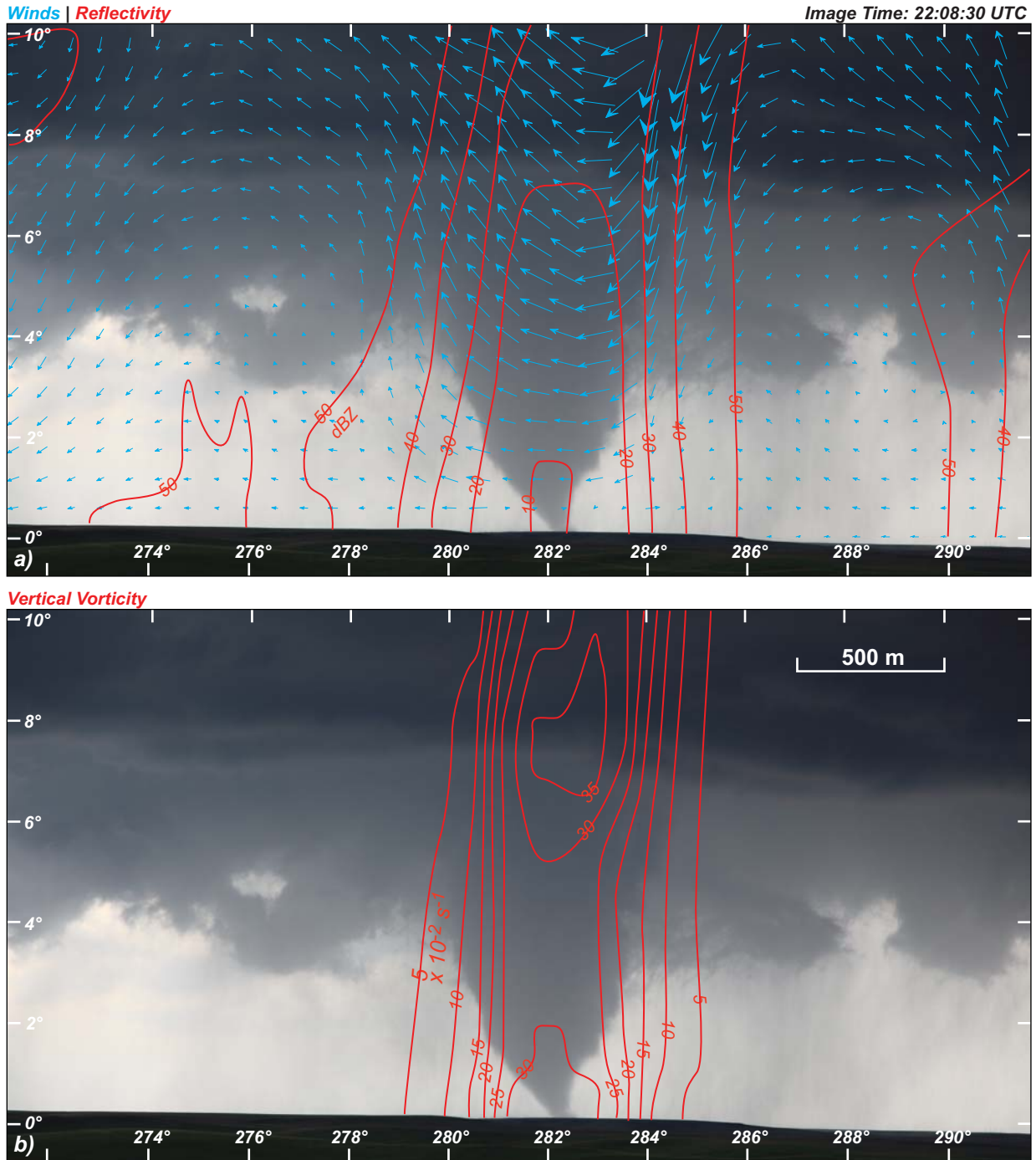


Fig. 5. Superposition of dual-Doppler data on a photograph taken at 22:08:30 UTC at the CAMA location in Fig. 2. (a) Winds in the plane of the cross section (blue) and radar reflectivity (red). (b) Vertical vorticity ($\times 10^{-2} \text{ s}^{-1}$), (c) divergence ($\times 10^{-2} \text{ s}^{-1}$), and (d) U component of the flow in the plane of the cross section are all shown in red. Zero lines in (c) and (d) are not plotted for figure clarity. Solid and dashed contours of (c) divergence and (d) U_r represent positive and negative values of the respective fields, respectively.

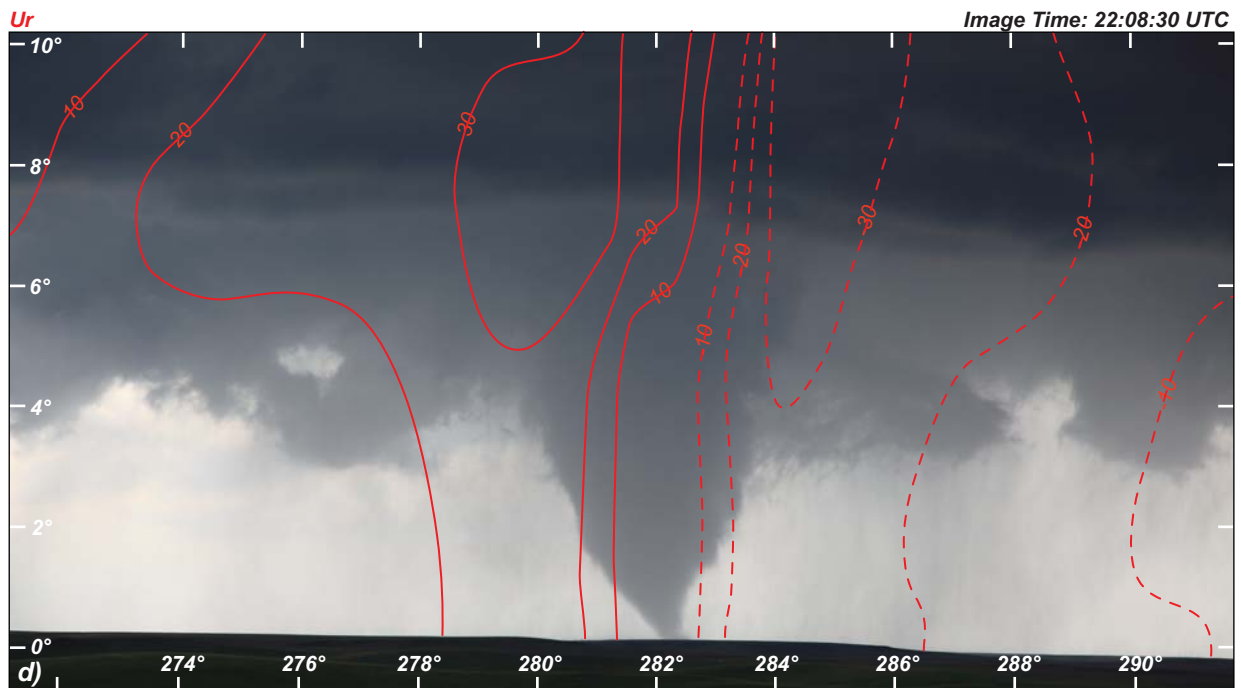
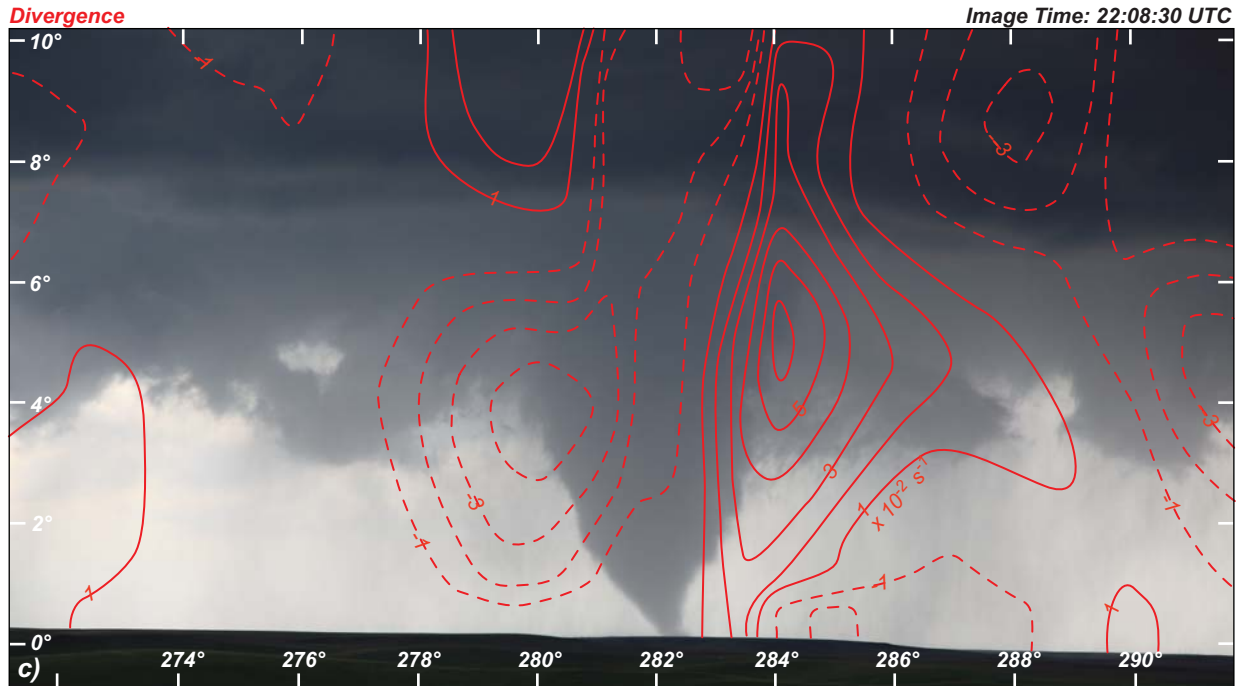


Fig. 5, continued.

mesocyclone within the hook region. These observations along with the horizontal vorticity distribution strongly suggested that baroclinic vorticity generation may play a role in the genesis of the vortex pair.

To see if a similar vortex line distribution was present within the hook region for the LaGrange tornado, vortex lines were computed and their two-dimensional positions are shown in Fig. 4b. Consistent with the Markowski et al. (2008) study, a few of the vortex lines on the periphery of the

cyclonic and anticyclonic vortices form arches and connect the two circulations through the observed cloud-base lowering. It is possible that some of the other vortex lines passing through the center of the vortices connect in the form of arches, however, the dual-Doppler data does not extend high enough to confirm this.

4. Low-level Winds at 22:08:30 UTC

In part I of this study, Wakimoto et al. (2010) documented a “double couplet” structure in the radial velocity field at 22:08 UTC. The lower couplet extended from the surface upward to about 200 m AGL. At this same altitude, the funnel was observed to abruptly widen. Wakimoto et al. (2010) hypothesized that the top of the narrow portion of the funnel demarcated the low-level inflow depth where convergence of swirling flow would lead to stronger low-level rotation.

Fig. 5 presents analyses that were produced to test the hypothesis put forth by Wakimoto et al. (2010) concerning the low-level funnel width relative to the radial inflow. The vertical vorticity field in Fig. 5b is consistent with strong low-level rotation near the ground and again above cloud base with local maxima at these locations. As would be expected, the vertical vorticity maxima are collocated with the funnel cloud. Interestingly, the U component of the wind field relative to the cross section orientation (Fig. 5d) shows the larger couplet above cloud base, however, the low-level couplet is not apparent. Furthermore, the wind field shown in Fig. 5a, does not clearly show the existence of radial inflow toward the funnel. The wind field appears to show downdraft and updraft on the northern and southern edges of the funnel, respectively. At low levels, the flow centered on the funnel appears to be weakly divergent (Figs. 5a, c). A weak-echo hole (Fig. 5a) was also collocated with the tornado funnel, as was discussed in detail by Wakimoto et al. (2010).

The results in Fig. 5 suggest that the dual-Doppler analysis may not be capturing the details of the low-level flow structure surrounding the funnel. This problem has been well documented in the literature and arises from the resolution of the radar pulse volume relative to the scale of the tornadic circulation and the centrifuging of scatterers from the tornado center (Dowell et al. 2005).

5. Relationship between Radius of Maximum Wind and Funnel Diameter

A fundamental question that has not been addressed in the literature is the location of the radius of maximum wind (RMW) relative to the observed funnel. The analysis in Fig. 6 attempts to address this issue.

The times shown in Fig. 6 correspond to when dual-Doppler volumes were collected by DOW 6 and 7 and the funnel was observed to be in contact with the ground. Notice that, with time, the funnel widens, especially near the ground. Also notice that the funnel tapers to smaller diameters closer to the ground.

The wind speed field, however, exhibits a much different structure. As would be expected, a minimum of wind speed is observed at the funnel center. The tornado appears to tilt with height, both to the south (Fig. 6a, f) and to the north (Fig. 6 d, e).

While the tornado funnel tapers to smaller diameters closer to the ground, the same is not true with the RMW. Near the ground, the RMW is much larger than the tornado funnel. While the tornado funnel widens with time near the ground, the RMW does not change appreciably during the time period shown in Fig. 6. At 22:05:58 UTC, the RMW is about 300m. By 22:12:03 UTC, it has decreased to 200 m and widens to about 260 m by 22:16:33 UTC. The width of RMW does not change appreciably with height for all times shown in Fig. 6. Near cloud base, however, the RMW is located approximately with the edge of the funnel (e.g., Fig. 6b, c, and d). The results in Fig. 6 suggest, that while the RMW may be located at the edge of the funnel near cloud base, this may not be true near the ground where the RMW may be located well beyond the location of the funnel cloud.

6. Angular Momentum and RMW

Within the supercell hook region, different scales of circulation have been discussed in the literature. They include the mesocyclone, the tornado cyclone, and the tornado. The relationship between these circulations, is not well understood. This can be partially attributed to the lack of high spatial and temporal observations of these circulations. While Doppler radars often well resolve the mesocyclone, this is not always true for the tornado cyclone and tornado due to their small spatial scales.

Angular momentum was used by Rasmussen and Straka (2007) to define the spatial scale of the tornado cyclone observed within a significant tornadic supercell at close range by a mobile Doppler

5 June 2009

Horizontal Wind Speed

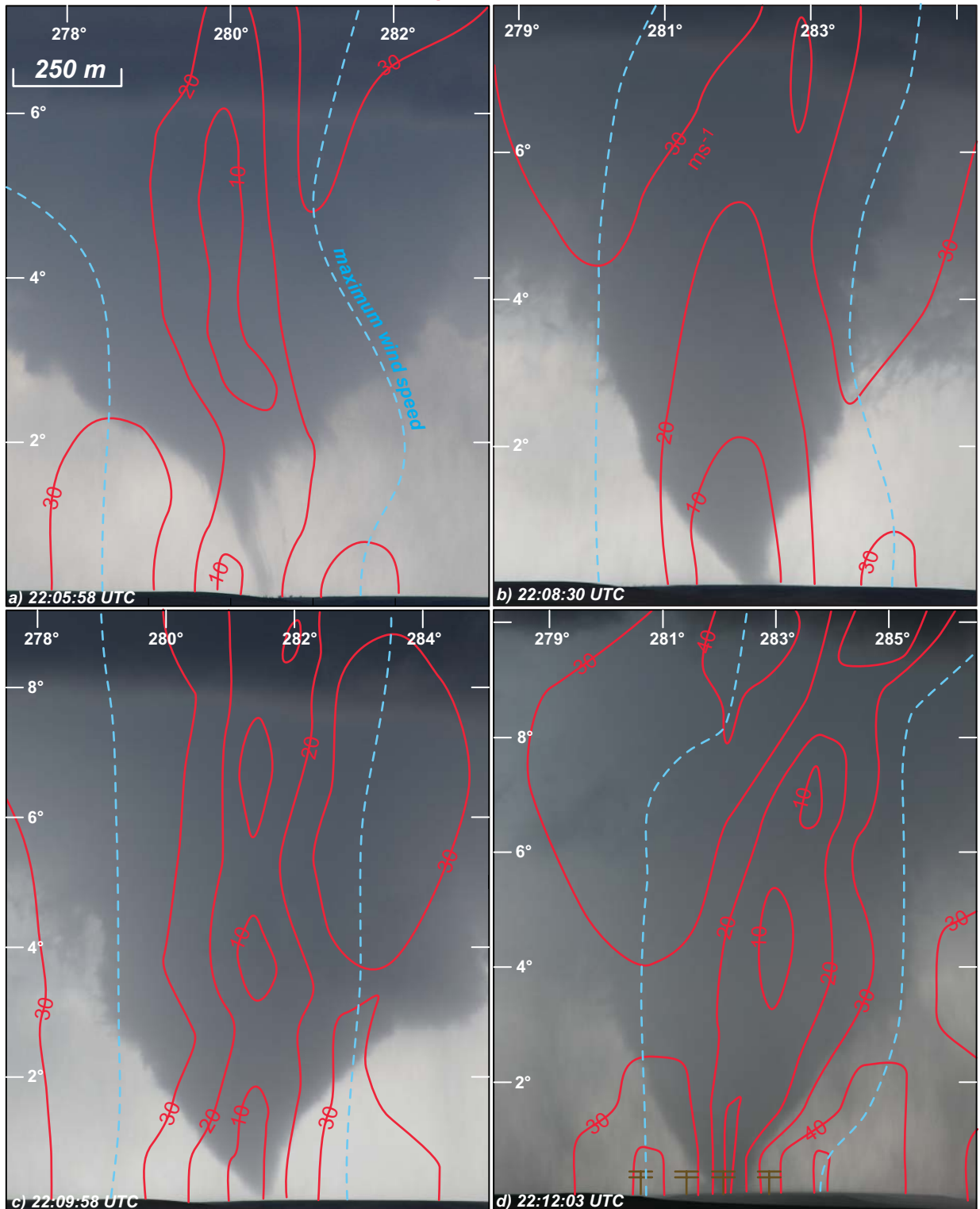


Fig. 6. Vertical cross sections of wind speed (ms^{-1} , red) at a) 22:05:58, b) 22:08:30, c) 22:09:58, d) 22:12:03, e) 22:14:01, and f) 22:16:23 UTC. The location of maximum wind speed is shown by the dashed blue lines. The radar data is along the plane of the photo and passes through the vertical vorticity maximum. The telephone poles in (d) represent the approximate locations of the damage poles shown in the central panel in Fig. 2.

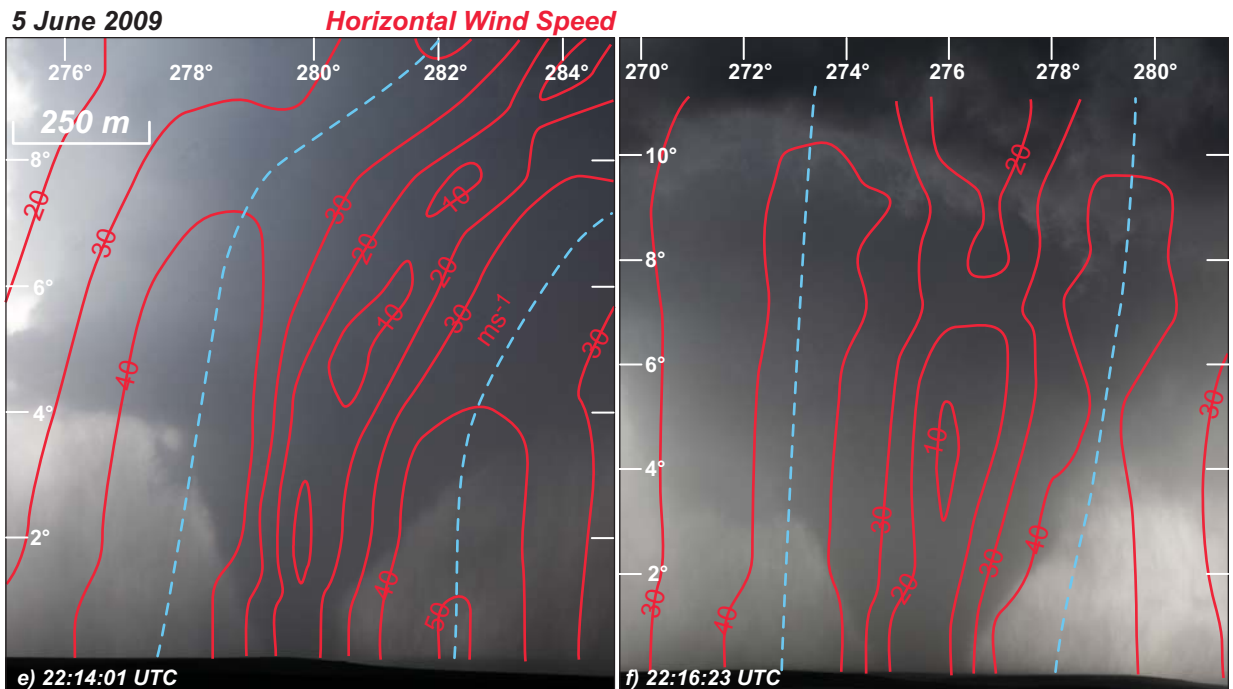


Fig. 6, continued.

radar. To examine the relationship between the mesocyclone, tornado cyclone, and tornado with the 5 June 2009 LaGrange, WY tornado, the azimuthally averaged angular momentum field was computed and superimposed on photos of the wall cloud and funnel from 21:58:21 to 22:16:23 UTC in Fig. 7. Also plotted in Fig. 7 is the location of the RMW. The angular momentum field undergoes a dramatic evolution in the time period shown in Fig. 7. At 21:58:21 UTC, angular momentum shows little vertical variation and increases linearly outward from the center of the wall cloud and mesocyclone. Notice that the largest values of angular momentum for the times shown in Fig. 7 are observed at 21:58:21 UTC. Four minutes later (Fig. 7b), the largest values of angular momentum have shifted to low levels below cloud base and to large radii from the circulation center. Azimuthally averaged winds (not shown) were observed to transport this high angular momentum air inward to the circulation center. Furthermore, the radial extent of the linear increase of angular momentum appears to be approximately located at the wall cloud edge. This observation suggests that the angular

momentum field is capturing the mesocyclone-scale circulation. This distribution of angular momentum is apparent four minutes later at 22:05:58 UTC, the time the funnel was observed continuously in contact with the ground. From 22:08:17 UTC (Fig. 7d) to 22:16:23 UTC (Fig. 7f), the angular momentum distribution undergoes a dramatic evolution. The radial gradient of angular momentum increase at 22:08:17 UTC has weakened slightly relative to earlier times. This trend continues through 22:16:23 UTC where the radial gradient of angular momentum is the weakest of all times shown in Fig. 7. At the same time, the funnel diameter continued to get larger from 22:05:58 through 22:16:23 UTC. This observation suggests that low-level, radially inward transport of high angular momentum air can not explain the apparent intensification of the tornado at the later times in Fig 7d-f). The edge of the radial increase of angular momentum continues to be approximately collocated with the wall cloud edge (Fig. 7d).

If the RMW approximately delineated the spatial scale of the tornado, the results in Fig. 7 suggest that only two scales of circulation were

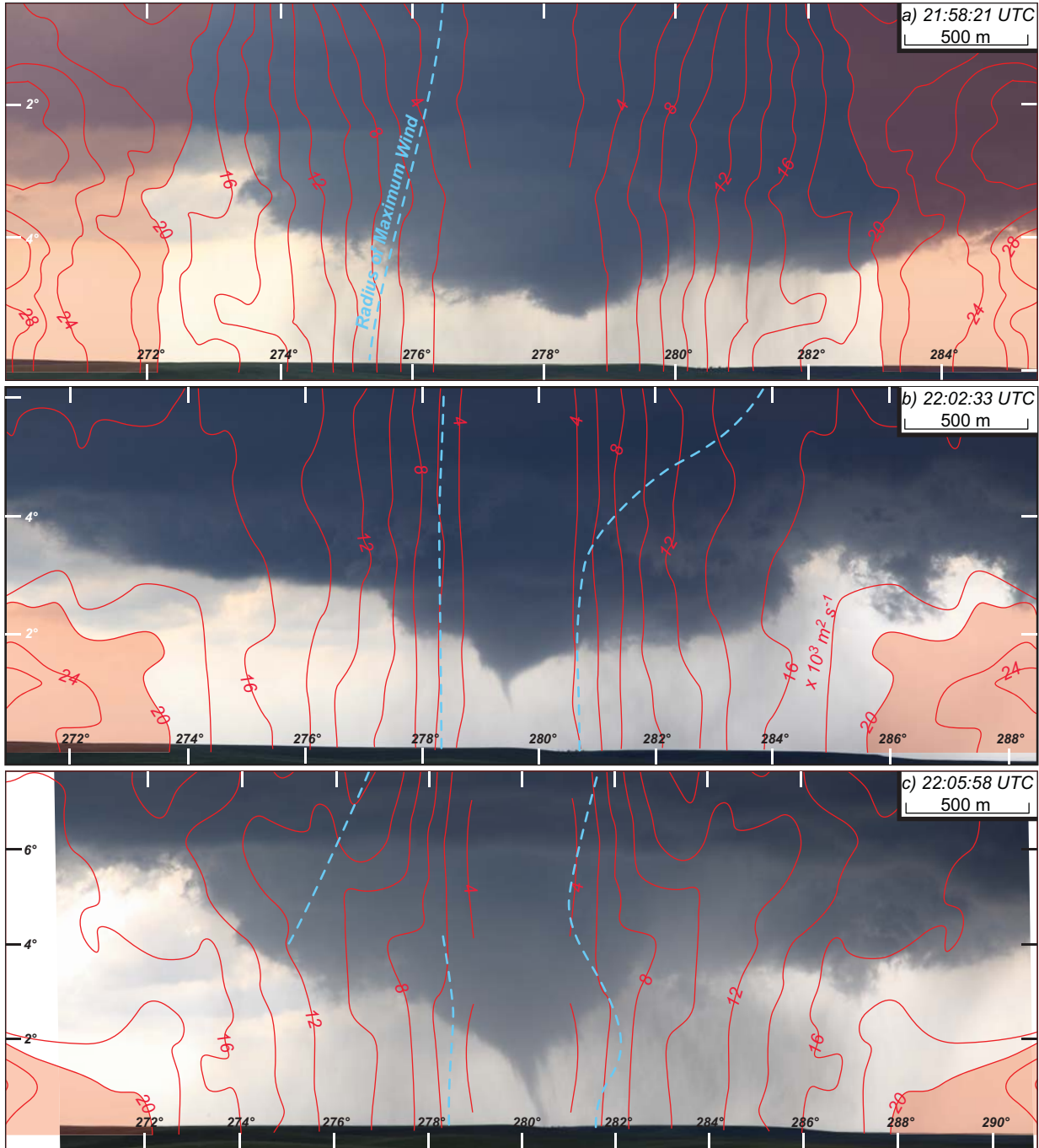


Fig. 7. Vertical cross sections of angular momentum ($\times 10^3 \text{ m}^2 \text{ s}^{-1}$) in red with values greater than $20 \times 10^3 \text{ m}^2 \text{ s}^{-1}$ shaded at a) 21:58:21, b) 22:02:33, c) 22:05:58, d) 22:08:17, e) 22:12:03, and f) 22:16:23 UTC. Similar to Fig. 6, dashed blue lines are the locations of maximum wind speed. The brown symbols in d) represent the approximate locations of the snapped telephone poles shown in Fig. 2.

present. They are the tornado and mesocyclone, as delineated in photos by the lowered cloud base and in the angular momentum field. There is no

evidence of a tornado cyclone in the data shown in Fig. 7.

7. Summary and Conclusions

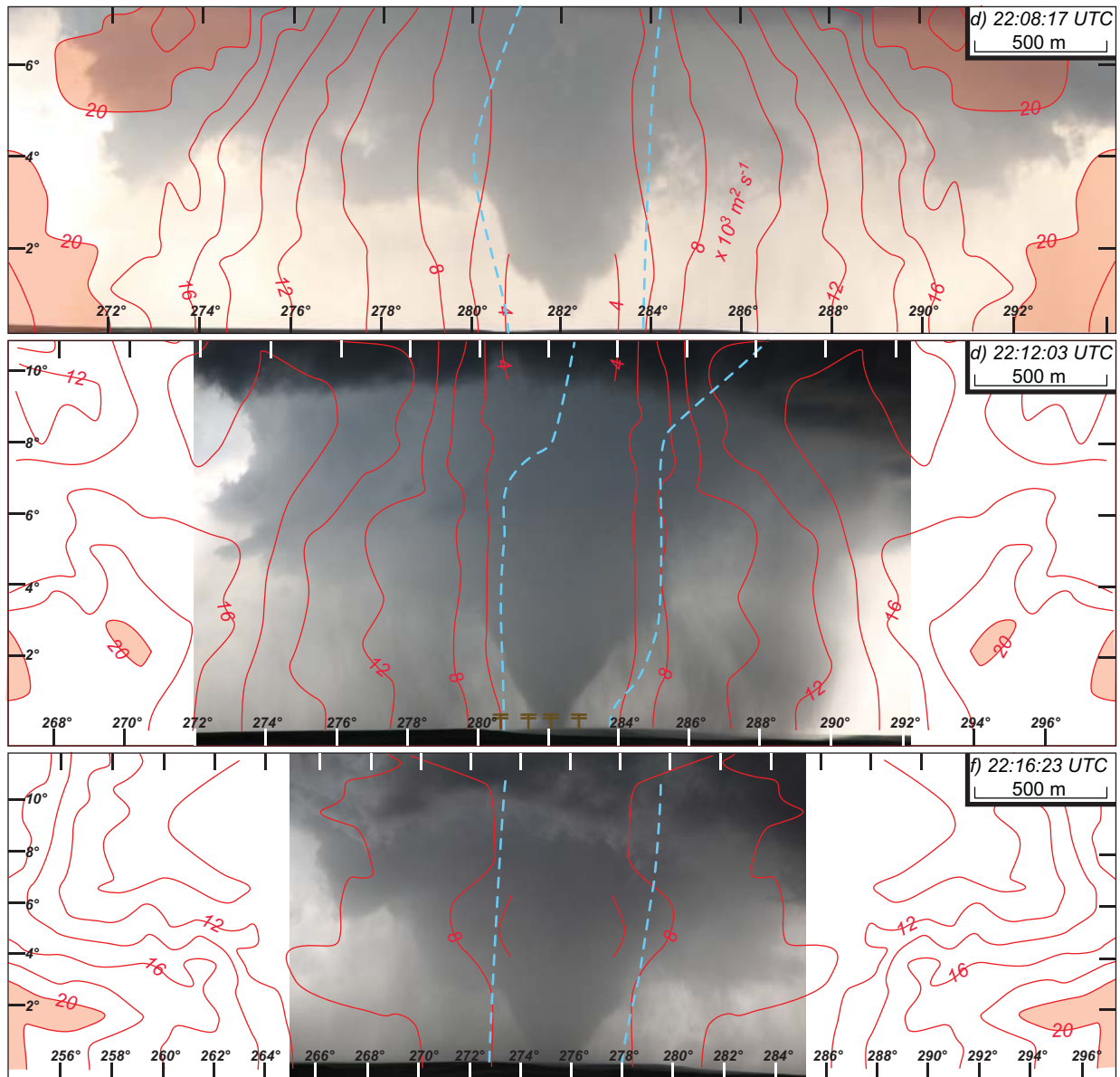


Fig. 7, continued.

Detailed analyses combining mobile dual-Doppler data with photogrammetrically analyzed photographs of the 5 June 2009 LaGrange tornado have been presented. The analyses have focused on relating the visual features observed in the hook region with the dual-Doppler data. The preliminary findings of this study are as follows.

1. At the time of radar-determined tornadogenesis, no funnel was observed. In fact, 11 minutes elapsed from tornadogenesis until the time that the

funnel was observed to be continuously in contact with the ground.

2. Much of the initial tree damage occurred during and just after tornadogenesis. The damage was observed to be located just south of the east south-eastward moving vortex and in the rear-flank downdraft.

3. Two cloud-base lowerings were observed at the time of tornadogenesis. A smaller anticyclonic lowering was observed to the south of the larger cyclonic wall cloud. Vortex lines originating on the periphery of the cyclonic circulation pointed

upward, arched southward, and pointed down into the anticyclonic circulation. This result is consistent with the results of Markowski et al. (2008) who showed a similar pattern of vortex lines within supercells. The result suggests that baroclinic generation of vorticity is responsible for the genesis of the circulations.

4. A few minutes after the funnel was observed continuously on the ground, the funnel diameter discontinuously tapered to smaller values close to the ground. A single-Doppler analysis revealed an intense low-level rotational couplet having a depth similar to the tapered portion of the funnel. It was hypothesized that the couplet represented low-level swirling inflow that then turned upward and diverged at the top of the narrowed portion of the funnel. Dual-Doppler data at the same time of the single-Doppler observations could not confirm this hypothesis and called into question how representative the low-level dual-Doppler data is of the actual low-level tornadic wind field.

5. The radius of maximum wind was plotted on photographs when the funnel was continuously on the ground. Near cloud base, the RMW was located on the edge of the condensation funnel. Closer to the ground, the RMW did not change. It remained approximately constant with height even though the funnel tapered to smaller diameters near the ground. Therefore, the RMW was located well beyond the funnel edge near the ground.

6. Azimuthally averaged angular momentum was plotted on photographs of the wall cloud and funnel. The largest values of angular momentum were observed at earlier times, well before the condensation funnel was visible. It is hypothesized that radial inflow advected the larger angular momentum air inward allowing the circulation to intensify. Once the condensation funnel was visible, the largest angular momentum was observed below cloud base and outside the mesocyclone circulation. The angular momentum field appeared to reveal the existence of the mesocyclone; no tornado cyclone was evident in the data. At later times, the angular momentum gradient weakened while the funnel diameter increased suggesting that conservation of angular momentum was less important at intensifying the circulation.

Acknowledgements.

Research results presented in this paper were supported by the National Science Foundation under Grant ATM-0757714. The National Center

for Atmospheric Research is sponsored by the National Science Foundation. Any opinions, findings and conclusions or recommendations expressed in this publication are those of the authors and do not necessarily reflect the views of the National Science Foundation. The DOW radars are National Science Foundation Lower Atmospheric Observing Facilities supported by ATM-0734001. The DOW deployments in VORTEX2 have been supported by ATM-0910737 and ATM-0966095. Analysis of DOW data has been supported by ATM-0947235. VORTEX2 has been supported, in part, by ATM-0724318.

REFERENCES

- Abrams, T., 1952: *The manual of photogrammetry*. George Banta Publishing, 876 pp.
- Alexander, C.R., and J. Wurman, 2005: The 30 May 1998 Spencer, South Dakota storm. Part I: The structural evolution and environment of the tornadoes. *Mon. Wea. Rev.*, **133**, 72-96.
- Bluestein, H.B., J.G. LaDue, H. Stein, D. Speheger, and W.P. Unruh, 1993: Doppler radar wind spectra of supercell tornadoes. *Mon. Wea. Rev.*, **121**, 2200-2221.
- _____, W.P. Unruh, D.C. Dowell, T.A. Hutchinson, T.M. Crawford, A.C. Wood, H. Stein, 1997: Doppler radar analysis of the Northfield, Texas, tornado of 25 May 1994. *Mon. Wea. Rev.*, **125**, 212-230.
- _____, C.C. Weiss, A.L. Pazmany, 2004: The vertical structure of a tornado near Happy, Texas, on 5 May 2002: High-resolution, mobile, W-band, Doppler radar observations. *Mon. Wea. Rev.*, **132**, 2325-2337.
- _____, C.C. Weiss, M.M. French, E.M. Holthaus, R.L. Tanamachi, S. Frasier, and A.L. Pazmany, 2007a: The structure of tornadoes near Attica, Kansas, on 12 May 2004: High-resolution, mobile, Doppler radar observations. *Mon. Wea. Rev.*, **135**, 475-506.
- _____, M.M. French, R.L. Tanamachi, S. Frasier, K. Hardwick, F. Junyent, and A.L. Pazmany, 2007b: Close-range observations of tornadoes in supercells made with a dual-polarization, X-band, mobile Doppler radar. *Mon. Wea. Rev.*, **135**, 1522-1543.
- _____, D. Burgess, D. Dowell, P. Markowski, E. Rasmussen, Y. Richardson, L. Wicker, and J. Wurman, 2009: VORTEX2: The second verification of the origins of rotation in tornadoes

- experiment. Preprints, *5th European Conference on Severe Local Storms*, Landshut, Germany, O09-06.
- Dowell, D.C., C.R. Alexander, J.M. Wurman, and L.J. Wicker, 2005: Centrifuging of hydrometeors and debris in tornadoes: Radar-reflectivity patterns and wind-measurement errors. *Mon. Wea. Rev.*, **133**, 1501-1524.
- Holle, R.L., 1986: Photogrammetry of thunderstorms. *Thunderstorms: A Social and Technological Documentary*, 2d ed., E. Kessler, Ed., Vol. 3, University of Oklahoma, 77-98.
- Markowski, P., E. Rasmussen, J. Straka, R. Davies-Jones, Y. Richardson, and R. J. Trapp, 2008: Vortex lines within low-level mesocyclones obtained from pseudo-Doppler radar observations. *Mon. Wea. Rev.*, **136**, 3513-3535.
- Rasmussen, E.N., R. Davies-Jones, and R.L. Holle, 2003: Terrestrial photogrammetry of weather images acquired in uncontrolled circumstances. *J. Atmos. Oceanic Technol.*, **20**, 1790-1803.
- _____, E., and J.M. Straka, 2007: Evolution of low-level angular momentum in the 2 June 1995 Dimmitt, Texas, tornado cyclone. *J. Atmos. Sci.*, **62**, 2037-2057.
- Wakimoto, R.M., N.T. Atkins, and J. Wurman, 2010: The LaGrange Tornado during VORTEX2. Part I: Photogrammetric Analysis of the Tornado Combined with Single-Doppler Radar Data. submitted to *Mon. Wea. Rev.*
- Wurman, J., and S. Gill, 2000: Finescale radar observations of the Dimmitt, Texas (2 June 1995), tornado. *Mon. Wea. Rev.*, **128**, 2135-2164.
- _____, J., 2001: The DOW mobile multiple-Doppler network. Preprints, *30th Int. Conf. on Radar Meteorology*, Munich, Germany, Amer. Meteor. Soc., CD-ROM, P3.3.
- _____, J.M. Straka, and E.N. Rasmussen, 1996: Fine-scale Doppler radar observations of tornadoes. *Science*, **272**, 1774-1777.
- _____, Y. Richardson, C. Alexander, S. Weygandt, and P.F. Zhang, 2007a: Dual-Doppler and single-Doppler analysis of a tornadic storm undergoing mergers and repeated tornado genesis. *Mon. Wea. Rev.*, **135**, 736-758.
- _____, _____, _____, _____, and _____, 2007b: Dual-Doppler analysis of winds and vorticity budget terms near a tornado. *Mon. Wea. Rev.*, **135**, 2392-2405.
- Zehnder, J.A., J. Hu, and A. Razdan, 2007: A stereo photogrammetric technique applied to orographic convection. *Mon. Wea. Rev.*, **135**, 2265-2277.